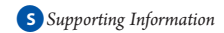# Plasmon-Assisted, Spatially Resolved Laser Generation of Transition Metal Oxides from Liquid Precursors
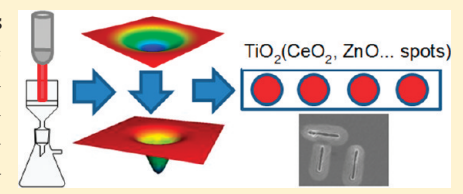
Ivano Alessandri,*,† Matteo Ferroni,‡ and Laura E. Depero†

†INSTM and Chemistry for Technologies Laboratory, University of Brescia, via Branze 38, 25123 Brescia, Italy

‡CNR-IDASC Sensor Laboratory and Department of Chemistry and Physics for Materials and Engineering, University of Brescia, via Valotti 9, 25123 Brescia, Italy

Ⓢ *Supporting Information*

ABSTRACT: Plasmonic heating-triggered laser generation of nanocrystalline oxides on colloidal crystal substrates has been so far limited by deposition of the oxide precursors, which relies on chemical vapor methods. A novel approach, based on infiltration of liquid precursors and characterized by a good control of spatial localization, was reported in this paper. Patterning of titanium oxide spots and microchannels was successfully performed. Additional advantages were highlighted by extending this procedure to oxides, such as ZnO and CeO₂, which are otherwise difficult to generate on these substrates by traditional approaches. Raman microspectroscopy evidenced the highly defective, nanocrystalline nature of the oxides. Scanning electron microscopy provided further microstructural information that allowed us to gain more insight into the mechanisms that govern the formation of these oxide spots and channels.

■ INTRODUCTION

Laser-assisted synthesis of nanoparticles and nanostructures is a widespread, inter- and cross disciplinary topic which has a strong impact on several fields of materials science and nanotechnology.[1] Along with traditional pulsed-laser deposition (PLD) methods, which are based on laser ablation of a solid target at a solid/gas interface in a vacuum chamber, a number of novel approaches have been recently proposed to perform laser ablation at solid/liquid interfaces.[2−6] These methods are, in general, very simple and yield nanocrystals which do not need any further modifications. Moreover, metastable materials can be directly achieved, without need of either high-pressure or hydrothermal techniques.[7]

Another topical issue is given by direct laser modification of functional substrates. In general, targets used for ablation are bulk materials which play just as a source or as precursors of the final products. However, for some applications, it could be important to induce laser-mediated processes (including ablation, melting, chemical reactions, polishing...) directly on specific sites of the target substrate. For example, there is a great interest in achieving microcontainers and microreactors for in situ, real-time monitoring of various chemical and physical events, such as catalytic reactions, phase transitions, biochemical interactions, and self-healing interfaces.[8−10] In this context, the extremely localized nature of laser heating can be very helpful to restrict and control irradiation effects on selected areas. Another major asset could be achieved by focusing the laser through the objectives of an optical microscope. In this case, the advantage is 2-fold. On one hand, the power of the laser radiation can be concentrated within a small area, allowing us to achieve ablative effects even by means of low-power, continuous wave (c.w.) lasers equipped in standard Raman microscopes.[11] In addition, optical inspection and precision in positioning, which are mandatory in view of patterning of arrayed microwells or microfluidic channels, are directly attainable. On the other hand, this experimental setup is inherently suitable for either Raman or infrared microspectroscopy. In particular, the development of oxide-based patterned arrays which can be exploited for Surface Enhanced Raman Spectroscopy (SERS) promises to be a powerful tool for analytical purposes[12] and fundamental studies.[13] In recent years, we demonstrated that anatase micrometer-sized spots can be patterned on the surface of colloidal crystals by direct laser irradiation. Two different approaches were explored. In one case, the substrates were made of gold nanoshells (i.e., polystyrene/Au core/shell nanospheres) coated by a thin layer of amorphous titania.[14] In another approach, gold nanoparticle agglomerates were dispersed onto titania nanoshells.[15] In both cases, plasmonic heating effects resulting from interaction between a c.w. He−Ne laser and gold nanostructures allowed us to induce anatase crystallization at specific sites. Localized generation of anatase inverse opals[16] as well as plasmonic heating-assisted deposition of bare Au nanoparticles onto titania nanoshells[17] were also obtained by optimizing the size of colloids and using a laser scanning procedure, respectively. The presence of gold made all of these sites SERS-active, allowing photocatalytic reactions to be monitored. However, some limitations to the extensive use of

---

these laser-modified substrates still exist. In particular, a major drawback is due to the metal oxide generation. In fact, in all of the above-mentioned examples, titania shells were obtained by atomic layer deposition (ALD), which is an excellent tool for yielding very conformal coatings with nanometric or subnanometric control of the film thickness.[18,19] Unfortunately, ALD processes are quite slow (in our case it takes about 5 h for growing 100 nm of TiO_2) and limited by precursor availability. ALD precursors are in general based on metal—organic compounds, so they are very expensive and/or hazardous in most of the cases. Moreover, in view of generating SERS active metal oxide spots onto colloidal crystals, only a very small area of the substrate needs to be coated, which implies that deposition stage wastes large amounts of precursors. In addition, the plasmonic heating-assisted generation of SERS active substrates should be extensible to a wide range of important transition metal oxides. However, most of them do not have any suitable precursors for ALD, or they cannot be deposited under mild conditions as such required by polymeric colloidal crystals (deposition temperature below 100 °C). For example, the ALD precursors of an extremely important catalytic material such as ceria[20] are working only above 175 °C.[21] Moreover, incomplete deposition of the ALD precursors yields organic moieties that contaminate the substrate surface, so that spectroscopy experiments could be severely affected. For other important oxides, such as ZnO, ALD allows us to grow nanocrystals at quite low temperatures (60—90 °C).[22] In this case, the overall effect of laser processing is more similar to that of a local annealing, which gives rise to specific sites characterized by a higher degree of ZnO crystallinity. This makes it difficult to distinguish the laser-treated regions from the as-deposited ZnO background, so that spectroscopy studies of these sites may yield unreliable data.

Finally, optothermal conversion of laser irradiation should transform amorphous phases into crystalline or partially crystalline oxides (laser-induced amorphization upon rapid undercooling is not desirable because, in general, catalytic reactions and electron-transfer processes that have to be studied on these sites are more efficient in crystalline compounds). Thus, only the irradiated portion of the colloidal crystal substrate should crystallize, to facilitate the in situ monitoring of the processes under investigation.

In this paper, a novel approach, based on direct infiltration of oxide precursors into gold-coated colloidal crystals and their subsequent plasmonic heating-assisted local crystallization, is reported. We demonstrated that the mechanisms underlying the laser generation of nanocrystalline oxides are still working in the present case and can be exploited to control the structure and morphology of the resulting products, which were comparable to those achieved by methods based on chemical vapor processes. The successful generation of critical oxides, such as CeO_2 and ZnO, confirmed the potential advantages of this method, which was also tested in view of introducing patterned microchannels on the surface of the colloidal crystals (AuCCs), opening the way to novel applications of these materials.

■ EXPERIMENTAL SECTION

Materials. Monodisperse polystyrene (PS) nanospheres (diameter: 150 ± 6 nm) suspended in Milli-Q water (10 wt %) were purchased from MicroParticles GmbH and sonicated before use. Titanium(IV)-isopropoxide (98%), zinc acetate dihydrate (99%), cerium(III) nitrate hexahydrate (99.5%), citric acid (98%),

ethanol (99.8% v/v), and concentrated hydrochloric acid (37% wt) were obtained from Aldrich and used as received without further purification.

Preparation of Au-Coated Colloidal Crystals (AuCCs) and Formation of Nanocrystalline Oxides. The AuCCs used for these experiments were prepared according to ref 11. Briefly, multilayered colloidal crystals were assembled by sedimentation of the aqueous suspension of monodisperse PS nanospheres.[23-] The resulting colloidal crystals were dried at 60 °C overnight then heated at 120 °C for 1 min to yield partial melting of the spheres at their contact points. This procedure improved mechanical stability of the colloidal crystals during infiltration. The colloidal crystals were then coated with a thin layer of gold (about 10 nm) by d.c. sputtering at room temperature (discharge current, 35 mA; total pressure, 10^{-1} mbar). This procedure yielded closely aggregated gold nanodomains.[11,14] The optical characterization of these systems has been reported elsewhere.[16] Solutions (0.01 M) of the precursors in ethanol were used in the infiltration stage. Typical preparations of the metal oxide precursors were carried out by dissolving: (a) titanium(IV) isopropoxide (0.028 g) in ethanol (8 mL) and HCl (2 mL), (b) cerium nitrate hexahydrate (0.043 g) and citric acid monohydrate (0.021 g) in ethanol (10 mL), and (c) zinc acetate dehydrate (0.022 g) in ethanol (10 mL). Infiltration was performed by pouring the precursor solution onto dried AuCCs placed in a Büchner funnel that is connected with a vacuum line. The nanocrystalline oxides were generated by direct laser irradiation of the infiltrated AuCCs, which were set upon the motorized x—y stage (resolution, 0.1 μm; scanning range, 100 × 100 mm) of a Raman microscope (Labram HR800, Horiba/Jobin-Yvon). The spots were obtained by focusing a continuous wave (c.w.) He—Ne (λ = 632.8 nm) laser through a 50× long-working distance objective (NA: 0.5) at different exposure time (from 1 to 300 s). The nominal power of the unfiltered laser radiation incident on the sample was about 5 mW. Extended tracks were obtained by scanning the laser over the substrate surface (scanning rates: 1 and 0.1 μm/s) with a 50× long-working distance objective (NA: 0.5).

Structural and Microstructural Characterization. The same high-resolution micro-Raman spectrophotometer previously used to generate the oxides was exploited for their structural characterization. The Raman spectra were acquired by means of optical filters that attenuated the power of the laser to 0.05 mW. This precaution prevented introduction of further thermal effects during Raman acquisition. Spectra were acquired for 120 s with a 100× (N.A.: 0.9) objective, to offset the low Raman intensity due to use of optical filters. The scanning electron microscopy (SEM) images were carried out by an LEO 1521 high-resolution instrument equipped with a field emission gun and in-lens secondary electron detector.

■ RESULTS AND DISCUSSION

Laser Irradiation of Precursor-Infiltrated AuCCs. Figure 1a shows the results of laser irradiation of Au-coated colloidal crystals (AuCCs) infiltrated with a titanium isopropoxide solution. During infiltration, a laser was focused through the 50× objective of a Raman microscope. The estimated output power of the laser was 5 mW, corresponding to about 6.5×10^5 W/cm^2 or 1.4×10^{16} photons/s μm^2 on the sample. Laser irradiation yielded circular spots, characterized by central features which are surrounded by halos, whose size is proportional to the exposure time. The only exception is represented by the 1s spot, where just
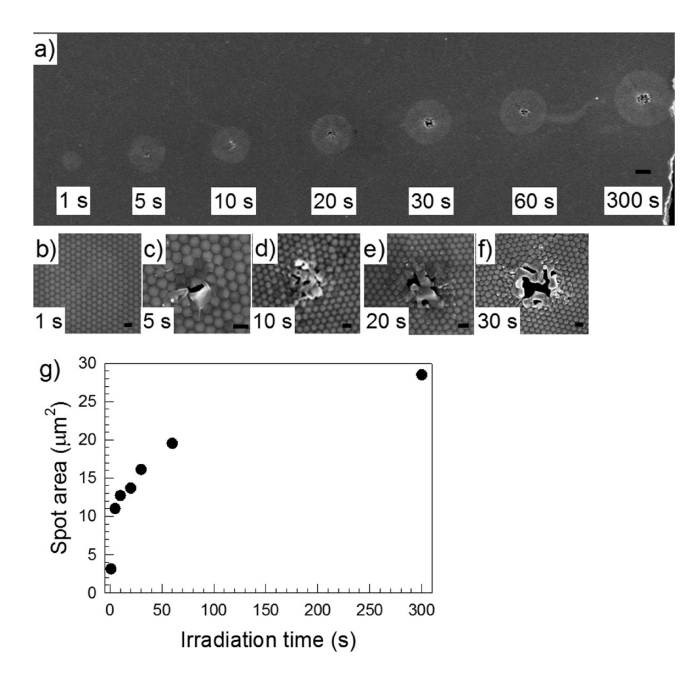
Figure 1. (a) SEM image showing the effects of laser irradiation at different exposure time (substrate, AuCCs infiltrated with titania precursors; scale bar, 2 μm). (b−f) High-magnification images showing the central regions of different spots (scale bars: 200 nm). (g) Plot of spot size (the bright halos of Figure 1a; error bars are included in dot size) as a function of the irradiation time.

a halo is observed. Analogous results were obtained with the other precursors. The general morphology of these spots is similar to that of ALD-coated AuCCs prepared using polystyrene cores of the same size (150 nm), yet in that case even localized inverse opal nanostructures were generated under particular conditions.[16] Thus, an analogous mechanism is expected to govern their formation. Also in the present case the laser beam penetrates the precursor overlayer and is strongly absorbed by the gold interlayer, which is a very efficient photon−thermal converter and plays as a secondary source of heat.[14] As the thermal conductivity of the underlying polystyrene cores is very low (~0.15 W/mK), heat cannot be dissipated in an effective way, leading local temperature to increase up to the thermal decomposition of the polymeric spheres. The latter process is exothermic, so further heating is developed, contributing to drive the formation of nanocrystalline oxides from precursors (see the Raman spectra reported below).

A closer inspection of these spots, provided by higher magnification SEM images (Figures 1b−f), shows that a small central hole is generated upon irradiating for a few seconds (as can be seen in the 5s spot, Figure 1c) and expands for longer exposures (see, for example, Figures 1d−f). The overall size and shape of these spots reflect the Gaussian distribution of laser intensity across the substrate surface. The dependence of the halo size on irradiation time is plotted in Figure 1g. Hole formation is a key step to be taken into account to explain this trend. In general, heat exhibits a radial propagation across the surface of the sample. This provokes coalescence of the Au interlayer, which is evidenced by the appearance of the bright circular halos. Thus, the extension of these halos represents a sort of "footprint" of lateral heat propagation. When irradiation time is short enough to avoid the explosion of the polystyrene cores, heat propagation is almost completely restricted to the surface of the substrate. At this stage,

any nanocrystalline oxide phase cannot be formed and detected. However, upon explosion of the polystyrene cores, the laser can penetrate more deeply into the substrate, so that the surface thermal diffusion is significantly limited. In particular, the larger the size of the central hole (which implies higher absorption of the laser beam), the smaller the rate of lateral heat propagation. Further complications are introduced by the explosive nature of the processes that are responsible for generation of the central holes. Higher magnification images (in particular, Figures 1e and f) show that either single or multiple holes can be produced as outcomes of the core explosion. The boundary layers separating small multiple holes might act as gratings for scattering and diffraction of the incoming laser beam. In addition, the new-generated oxide layers might significantly limit the surface propagation of heat. Since all of these factors are convoluted and hard to be quantified separately, predictions of the lateral extension of heating effects suffer from some, yet small, uncertainties. However, for practical purposes, this is a negligible point because these spots aim to serve as active sites for microRaman experiments, and the lateral resolution of the probing lasers is usually more than 1 μm. From this standpoint, two separate spots, achieved by the same exposure time, have the same size and, more important, the same chemical and structural properties.

Raman Characterization. As already observed in the case of ALD-coated samples, the presence of gold nanoparticles is a key factor for enabling Raman detection of oxides generated by laser irradiation, whose thickness is usually very low. For example, in the case of ALD-coated nanoshells, Raman spectra were detected for titania layers less than 50 nm in thickness.[14,16] In our case, any direct measurements of thicknesses of the precursor layers which coat the AuCCs as a result of the infiltration processes could not be carried out. However, on the basis of both our previous works and literature data referring to preparations of inverse opals from liquid precursors,[24] we can estimate that the thickness of the precursor coatings is less than 50 nm. In addition, reference thin films of the three oxides, which have been grown onto glass substrates by direct heating of liquid precursors, did not exhibit any Raman detectable signals. On the contrary, the Raman spectra of the oxide spots resulting from laser irradiation of AuCCs (exposure time: 300 s) infiltrated with solutions of titanium isopropoxide, cerium nitrate, and zinc acetate were observed (Figures 2a−c). The spectra were acquired with an optical filter which attenuated the laser power down to 0.05 mW, to avoid any further laser-induced effects. Under these conditions, no detectable oxide signals were obtained from regions irradiated for 1 s, and in general, lower signals were observed for short-time irradiated areas. The extremely localized nature of the spots prevents their direct characterization by either laboratory diffraction techniques or TEM (in the latter case, it could be difficult to prepare the sample and find the region of interest; moreover, electron beam irradiation can induce further crystallization or significantly alter the specimen), so that Raman microspectroscopy is particularly suitable to obtain structural and microstructural information on the new-generated oxides.

The local formation of TiO_2 in the form of anatase is shown Figure 2a. $E_{g(1)}$, $B_{1g(1)}$, A_{1g} + $B_{1g(2)}$, and $E_{g(3)}$ Raman-active modes characteristic of anatase (space group: D_{4h}^{19}) appear at 154, 393, 513, and 638 cm^{-1}, respectively. In general, peaks are quite broad, as expected in the case of nanocrystalline titania. The $E_{g(1)}$ mode is used to be taken as an indicator of both size and stoichiometry of the anatase grains. In fact, the position and
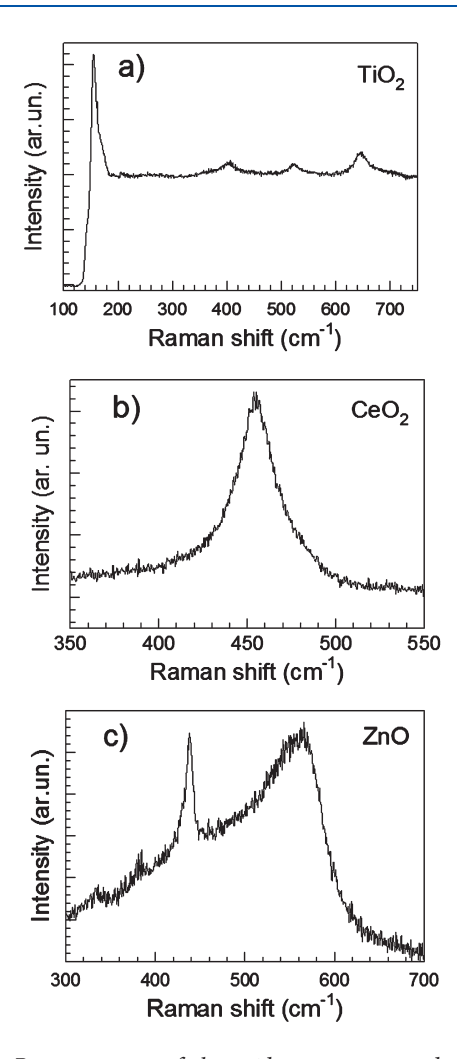
Figure 2. Raman spectra of the oxide spots generated upon laser exposure (300 s) of Au-coated colloidal crystals infiltrated with: (a) titanium isopropoxide, (b) cerium nitrate, and (c) zinc acetate solutions.

shape of this peak are particularly affected by both phonon confinement and increase of defect concentration, which are direct consequences of a reduced size of the grains.[25-27] Bulk anatase samples exhibit the $E_{g(1)}$ mode at 143–144 cm^{-1}. Phonon–phonon coupling increases as particle size decreases. As a consequence of the Heisenberg principle, given a nanoparticle of diameter D, the uncertainty $\Delta \kappa = \Delta p / \hbar$ on the wavevector must be above or equal to $(2D)^{-1}$. The phonon dispersion implies both asymmetric broadening and shift of this Raman peak. In particular, as the particle size decreases, the $E_{g(1)}$ mode shifts to higher frequency and asymmetrically broadens with a higher-frequency shoulder. These effects are observed also in the present case. The general equation which is used to express the Raman selection rule breaking and to quantitatively account for the spectral intensity and line shape is a weighted integral over the phonon frequency continuum around the Brillouin zone center:[25-28]

$$I(\omega) = \int \frac{|C(\mathbf{q})|^2}{[\omega - \omega(\mathbf{q})]^2 + (\Gamma_0/2)^2} \, d^3\mathbf{q} \qquad (1)$$

where $\mathbf{q}$ is the wave vector (expressed as π/a, where a is the unit cell parameter); $\omega(\mathbf{q})$ describes the dispersion relation of phonons in infinite crystals; and Γ_0 represents the width of the

Raman peak in infinite crystals (intrinsic mode line width). $C(\mathbf{q})$ is a weighting confinement function which corresponds to $\sim \exp(-q^2 D^2 / 8\beta)$, where D is the diameter of a spherical particle and β is the confinement factor, whose value depends on different boundary conditions used for calculations.

The quantitative predictions based on the phonon confinement model are strongly affected by fitting parameters which, in turn, depend on the rigidity of the initial confinement hypothesis. Due to this fact, data reported in the literature are somewhat different. However, a rough evaluation of grain size is enough for our purposes. On the basis of the model proposed by Zhu et al.,[28] in our case we can estimate a grain size of about 5 nm. However, it should be recalled that the phonon confinement model is a rough approximation for particles of this size range, and in general, it should not be applied below 5 nm, so that our data are close to the limits of applicability. In addition, the physical meaning of the D parameter should not be restricted to that of grain size, but it can be extended to any type of defect (twins, vacancies, stacking faults, inclusions, etc.) which may be active in phonon confinement. Thus, this value should be taken as a coherence length, which may indicate either the actual grain size or the existence of strain, nonhomogeneity of size distribution, or defects that, in the present case, can be due to oxygen vacancies and/or gold inclusions. Although Šćepanović et al. demonstrated that, in the case of sol–gel prepared anatase nanoparticles, phonon confinement effects predominate over strain and oxygen under stoichiometry,[29] their results cannot be extended to the present case, where rapid cooling and nonequilibrium conditions can play a major role. Similar arguments apply also for the remaining oxides.

The formation of nanocrystalline ceria with the typical fluorite-type cubic lattice is witnessed by the broad (fwhm: $\sim$27 cm^{-1}), slightly asymmetric F_{2g} peak around 455 cm^{-1}.[30] Like many other nanocrystalline materials, the line width of this mode is inversely proportional to the particle size. Following Kosacki et al.,[30] the estimated ceria grain size is about 7.5 nm. Assuming spherical symmetry of the grains, the corresponding correlation length, which identifies the average interdefect distance (viz., oxygen vacancies) in the oxygen lattice of ceria depends on the 1/3 power of the grain size. In the present case, the calculated correlation length is 1.9 nm. This value can be used to achieve a rough estimate of the concentration of oxygen vacancies (N)

$$N = \frac{1}{\frac{4}{3}\pi L^3} \qquad (2)$$

where L represents the correlation length. In the present case, the estimated concentration of oxygen vacancies was $\sim$3.5 × 10^{19} cm^3.

Finally, Figure 2c shows the Raman spectrum of the spot achieved upon irradiation of AuCCs infiltrated with zinc acetate. Raman modes at 334, 383, 438, and 565 cm^{-1} are observed. The first three signals are characteristic of ZnO with wurtzite structure (space group C_{6v}^4, $P6_{3mc}$). In particular, the signal at 334 cm^{-1} is attributed to second-order Raman scattering; the peak at 383 cm^{-1} is a polar $A_{1(TO)}$ mode; and the main peak, at 438 cm^{-1}, is a E_{2H} nonpolar phonon mode associated with oxygen sublattice. In addition, a broad, asymmetric band around 565 cm^{-1} indicates the presence of defects (interstitial Zn or, more likely in this case, oxygen vacancies).[31,32]

In summary, structural and microstructural data obtained by Raman microspectroscopy analysis point out that laser irradiation
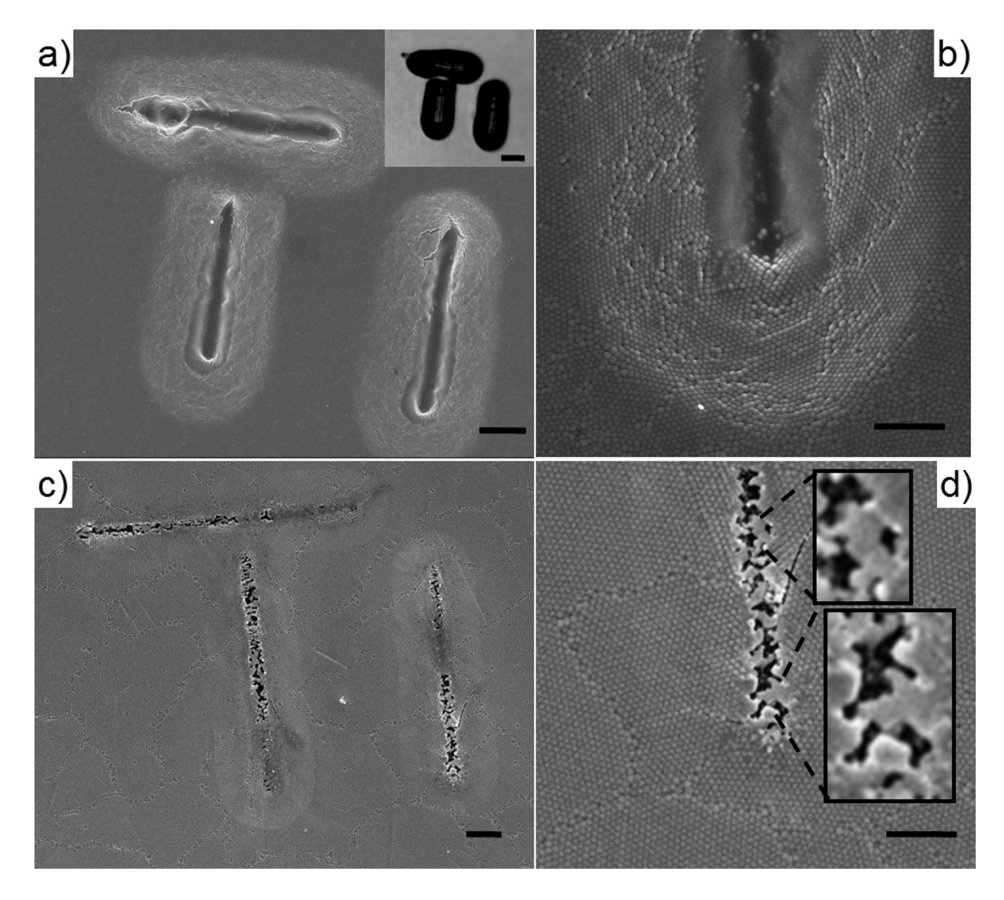
Figure 3. Written tracks generated upon laser scanning of Au-coated colloidal crystals infiltrated with titanium isopropoxide. (a) SEM image of the tracks achieved by scanning the laser at 1 μm/s. Inset: optical microscope image of the written colloidal crystal surface. (b) Magnification of image (a) showing details of the ablation track. (c) Tracks achieved by scanning the laser at 0.1 μm/s. (d) Magnification of image (c) showing details of the ablation track. Scale bars: 2 μm.

allows us to yield different types of oxides at specific, micrometer-sized regions of precursor-infiltrated AuCCs. In the present case, a rough evaluation of the local temperature, based on the intensity ratios of the Stokes and anti-Stokes Raman lines, is prevented by the continuous changes of surface morphology (and, as a consequence, of intensity) which occur during laser irradiation. However, some indications can be inferred from the highly defective, nanocrystalline nature of these oxides and comparisons with results obtained from bulk samples. We can assume that the thermal transport properties of the oxide precursors are quite similar with each other and play a minor role in influencing heat generation and propagation, which are dominated by the optothermal characteristics of the gold–polymer composite colloids. The thermal decomposition of polystyrene cores is expected to occur above 450 °C. The presence of oxide precursors and atmospheric oxygen might catalyze their decomposition at lower temperature, but the evidence of explosive effects indicates that the overall process reaches a high temperature in a very short time, as expected for laser-triggered events. Anatase is the lowest-temperature, thermodynamically stable titania polymorph and the preferential phase for titania nanostructures. In general, the onset of anatase crystallization is around 350 °C, and transformation into rutile does not occur before 500 °C. Although in some cases the anatase phase may be kept up to 800 °C, the grain size is expected to be much larger than that estimated by Raman analysis.[33] Analogous arguments can be applied also for CeO_2 and ZnO

phases. Highly defective ZnO nanocrystals are obtained by heating zinc-acetate precursors below 600 °C, whereas ceria Raman spectra similar to those achieved in the present experiment have been achieved by annealing cerium-nitrate precursors at 400 °C for 2 h.[31,34] On the other hand, the presence of a large number of oxygen vacancies can be strongly correlated to the short process time scale, so that a reliable evaluation of the average temperature is difficult to be made. However, the important parameter is the "phenomenological temperature", which is the temperature requested to obtain oxides with similar structural characteristics from direct heating of bulk precursors. In the present case, on the basis of the Raman data, we can conclude that laser irradiation gives rise to oxides similar to those achieved by heating their precursors in a range of 400–500 °C.

Surface Patterning by Laser Scanning. More complex 3D patterns can be generated through a laser scanning approach. This could be very important in view of preparing waveguides and SERS-active microreactors. Figure 3a shows an example of titania channels of arbitrary shape, achieved by scanning the He–Ne laser over the AuCCs surface (scanning rate, 1 μm/s; objective, 50×; N.A., 0.9). Other examples of surface patterns obtained from cerium and zinc-infiltrated AuCCs are reported in Supporting Information. The written tracks have both lateral and depth resolution of less than 2 μm. Previous laser scanning experiments, carried out onto ALD-coated colloidal crystals (AuCCs), yielded Au nanoparticles densely dispersed onto the borders of the laser track.[17] On the contrary, in the present case,

E

dx.doi.org/10.1021/jp110324y |*J. Phys. Chem. C* XXXX, XXX, 000–000

the borders are characterized by a continuous halo, analogous to that observed as a result of static irradiation which was used for generating spots. On the basis of those previous observations, we can conclude that the lateral propagation of heat produced by the laser moving source gives rise to coalescence of the intermediate gold layer, which remains embedded underneath the oxide precursor sheet (Figure 3b). Explosive processes, which were observed in the case of static generation of the oxide spots, were replaced by "softer" melting phenomena, which yielded a continuous oxide layer along the central part of the laser track.

Interestingly, different morphological effects can be achieved by slowing down the laser scanning rate. Figure 3c shows the effects achieved upon increasing dwell time (scanning rate: 0.1 μm/s). In this case, the written tracks are quite shallow and characterized by manifold central holes, indicating that explosive phenomena occurred at longer exposure time. Explosions strongly reduced homogeneity of heat generation and propagation, giving rise to discontinuous tracks. The latter showed evidence of nanoparticle sintering in their central part (see the zoomed image shown in Figure 3d). This experiment demonstrated once more that, like already observed in the case of static spot generation and in other previous works, exposure time is a key parameter, which should be carefully controlled to achieve reproducible effects.

In the present form, the laser scanning approach is not suitable for producing patterns on a large scale. A major limitation is represented by the manual approach, which makes the process quite time expensive. Precision and speed could be significantly improved through a process automation based on Computer Aided Design (CAD) of the patterns. Although far from being extended to large-scale applications, this approach can be exploited to prepare assays for monitoring different processes involving metal oxides, such as catalysis and surface interactions, and can be advantageous in comparison to other methods based on electron beam direct writing.[35]

CONCLUSION

This study demonstrated that important transition metal oxides can be directly generated by laser irradiation of Au-coated colloidal crystals impregnated with their liquid precursors. Static irradiation yielded circular spots, whereas dynamic laser scanning allowed us to obtain micrometer-sized channels. In both the cases, exposure time was a key parameter, which strongly affects spatial resolution, morphology, and microstructural characteristics of the resulting oxides. This approach represents a major breakthrough in solid state site-selective synthesis methods which are based on exploitation of plasmonic heating effects. In fact, it overcomes most of the limitations associated to these methods and provides a versatile, cheap, and fast alternative to atomic layer deposition and other chemical or physical deposition routes. Static irradiation can give rise to oxide spots with a large areal density ($\sim 10^6 - 10^7$ spots/cm^2). Laser scanning might be optimized to achieve microfluidic, SERS-active reactors. In general, the resulting materials can be valuable tools for studying manifold basic processes, including catalytic reactions and surface interactions, and their preparation strategy could be developed for fabrication of new multifunctional oxides.

ASSOCIATED CONTENT

ⓢ Supporting Information. Optical images of microchannels obtained using cerium and zinc precursor-infiltrated AuCCs. This material is available free of charge via the Internet at http://pubs.acs.org.

AUTHOR INFORMATION

Corresponding Author
*E-mail: ivano.alessandri@ing.unibs.it.

ACKNOWLEDGMENT

REFERENCES

(1) Barcikowski, S.; Devesa, F.; Moldenhauer, K. *J. Nanopart. Res.* **2004**, *11*, 1883.

(2) Amendola, V.; Meneghetti, M. *Phys. Chem. Chem. Phys.* **2009**, *11*, 3805.

(3) Mafune, F.; Kohno, J.; Takeda, Y.; Kondow, T.; Sawabe, H. *J. Phys. Chem. B* **2000**, *104*, 9111.

(4) Kazakevich, P. V.; Simakin, A. V.; Voronov, V. V.; Shafeev, G. A. *Appl. Surf. Sci.* **2006**, *252*, 4373.

(5) Yan, Z. J.; Bao, R. Q.; Chrisey, D. B. *Nanotechnology* **2010**, *21*, 145609.

(6) Besner, S.; Kabashin, A. V.; Winnik, F. M.; Meunier, M. *J. Phys. Chem. C* **2009**, *113*, 9526.

(7) Liu, P.; Cui, H.; Wang, C. X.; Yang, G. W. *Phys. Chem. Chem. Phys.* **2010**, *12*, 3942.

(8) Alessandri, I.; Depero, L. E. *ACS Appl. Mater. Interfaces* **2010**, *2*, 594.

(9) Heck, K. N.; Janesko, B. G.; Scuseria, G. E.; Halas, N. J.; Wong, M. S. *J. Am. Chem. Soc.* **2008**, *130*, 16592.

(10) Alessandri, I. *Small* **2010**, *6*, 1679.

(11) Alessandri, I.; Depero, L. E. *Nanotechnology* **2008**, *19*, 305301.

(12) Musumeci, A.; Gosztola, D.; Schiller, T.; Dimitrijevic., N. M.; Mujica, V.; Martin, D.; Rajh, T. *J. Am. Chem. Soc.* **2009**, *131*, 6040.

(13) Varaganti, S.; Ramakrishna, G. *J. Phys. Chem. C* **2010**, *114*, 13917.

(14) Alessandri, I.; Ferroni, M.; Depero, L. E. *ChemPhysChem* **2009**, *10*, 1017.

(15) Alessandri, I.; Depero, L. E. *Chem. Commun.* **2009**, *17*, 2359.

(16) Alessandri, I.; Ferroni, M. *J. Mater. Chem.* **2009**, *19*, 7990.

(17) Alessandri, I. *J. Colloid Interface Sci.* **2010**, *351*, 576.

(18) George, S. M. *Chem. Rev.* **2010**, *110*, 111.

(19) Alessandri, I.; Zucca, M.; Ferroni, M.; Bontempi, E.; Depero, L. E. *Small* **2009**, *5*, 336.

(20) Alessandri, I.; Banares, M. A.; Depero, L. E.; Ferroni, M.; Fornasiero, P.; Gennari, F. C.; Hickey, N.; Martinez-Huerta, M. V.; Montini, T. *Top. Catal.* **2006**, *41*, 35.

(21) Päiväsaari, J.; Putkonen, M.; Niinistö, L. *J. Mater. Chem.* **2002**, *12*, 1828.

(22) Alessandri, I.; Zucca, M.; Ferroni, M.; Bontempi, E.; Depero, L. E. *Cryst. Growth Des.* **2009**, *9*, 1258.

(23) Marlow, F.; Muldarisnur; Sharifi, P.; Brinkmann, R.; Mendive, C. *Angew. Chem., Int. Ed.* **2009**, *48*, 6212.

(24) Yan, H.; Blandford, C. F.; Holland, B. T.; Smyrl, W. H.; Stein, A. *Chem. Mater.* **2000**, *12*, 1134.

(25) Richter, H.; Wang, Z. P.; Ley, L. *Solid State Commun.* **1981**, *39*, 625.

(26) Campbell, H.; Fauchet, P. M. *Solid State Commun.* **1986**, *58*, 739.

(27) Arora, A. K.; Rajalakshmi, M.; Ravindran, T. R.; Sivasubramanian, V. *J. Raman Spectrosc.* **2007**, *38*, 604.

(28) Zhu, K. R.; Zhang, M. S.; Chen, Q.; Yin, Z. *Phys. Lett. A* **2005**, *340*, 220.

(29) Šćepanović, M. J.; Grujič-Brojčin, M.; Dokčević-Mitrović, Z. D.; Popovič, Z. V. *Appl. Phys. A* **2007**, *86*, 365.

(30) Kosacki, I.; Petrovsky, V.; Anderson, H. U.; Colomban, Ph. *J. Am. Ceram. Soc.* **2002**, *85*, 2646.

(31) Alessandri, I.; Bergese, P.; Depero, L. E. *J. Nanosci. Nanotechnol.* **2009**, *9*, 1597.

(32) Wu, J. J.; Liu, S. C. *J. Phys. Chem. B* **2002**, *106*, 9546.

(33) Li, W.; Bai, Y.; Liu, L.; Yang, Z.; Feng, X.; Xiaohua, L.; van der Laak, N. K.; Chan, K.-Y. *Environ. Sci. Technol.* **2009**, *43*, 5423.

(34) Audebrand, N.; Auffredic, J. P.; Louer, P. *Chem. Mater.* **1998**, *10*, 2450.

(35) Kern, P.; Müller, Y.; Patscheider, J.; Michler, J. *J. Phys. Chem. B* **2006**, *110*, 23660.